*Korean J. Chem. Eng.*, 38(6), 1149-1160 (2021)
DOI: 10.1007/s11814-021-0750-3

pISSN: 0256-1115
eISSN: 1975-7220

# Engineering of cobalt oxide-integrated nitric acid-functionalized Zr-$Fe_2O_3$ nanocoral photoanodes for photoelectrochemical water splitting

**Jun Beom Hwang*, Sarang Kim*, Weon-Sik Chae**, Habib Mohiddin Pathan***, Mahadeo Abasaheb Mahadik*,†, and Jum Suk Jang*,†**

*Division of Biotechnology, Safety, Environment and Life Science Institute, College of Environmental and Bioresource Sciences, Chonbuk National University, Iksan 54596, Korea
**Daegu Center, Korea Basic Science Institute, Daegu 41566, Korea
***Advanced Physics Laboratory, Department of Physics, Savitribai Phule Pune University, Pune-411007, India
(*Received 26 October 2020 • Revised 18 January 2021 • Accepted 26 January 2021*)

**Abstract**−A strategy involving $CoO_x$ catalyst adsorption and acid treatment for modifying the surface properties of Zr-doped hematite nanocoral (NC) photoanodes has been proposed. Acid-treated Zr-$Fe_2O_3$ NCs exhibited a reduced electrode/electrolyte interface resistance and improved surface charge-injection efficiency. X-ray photoelectron spectroscopy data confirmed an increased number of hydroxy groups and the formation of $Fe^{2+}$ sites on the surface of the acid-treated Zr-$Fe_2O_3$ NC, suggesting surface amendment. Furthermore, after surface amendment with a 1 mM $Co(OAc)_2$ solution, the $CoO_x$ encapsulated acid-treated Zr-$Fe_2O_3$ NC photoanode exhibited a photocurrent density of 1.83 mA/cm$^2$ at 1.23 V vs. RHE, following a 200-mV cathodic shift in the photocurrent onset compared with the bare Zr-$Fe_2O_3$ NC. The experimental results indicated the efficacy of acid treatment and $CoO_x$ adsorption for reducing the surface state and enhancing the photoelectrochemical water-oxidation performance. The acid-treatment step in the $CoO_x$-encapsulated acid-treated Zr-$Fe_2O_3$ NC provided a $CoO_x$ catalyst adsorption bond and permitted the kinetics of the charge-transfer process. This synergistic strategy of acid treatment and $CoO_x$ adsorption for enhancing the PEC performance provides a reference for accelerating the charge separation for other photoelectrodes.

Keywords: $CoO_x$ Adsorption, Nitric Acid Treatment, Zr-doped Hematite Nanocorals, Photoelectrochemical Water Oxidation

## INTRODUCTION

Photoelectrochemical water splitting has attracted considerable focus as a sustainable approach owing to its possible applications in answering the global energy crisis and reducing environmental pollution [1,2]. The main criteria for the photoelectrode in PEC are that it must exhibit conduction band and valence-band edges straddle with water reduction and oxidation potential and have excellent chemical stability in water, visible-light absorption, good charge-transport capability, good stability, and low production cost [3]. Amongst the previously studied semiconductors for water oxidation, small-bandgap metal-oxide semiconductors are particularly interesting because of their high visible-light activity and low cost [4]. Hematite ($\alpha$-$Fe_2O_3$) is a promising photocatalyst material owing to its narrow bandgap (2.1 eV), nontoxicity, and chemical stability [5]. However, $Fe_2O_3$ suffers from a low conduction-band bottom with respect to the water reduction level [6], a truncated carrier mobility (<1 cm$^2$ V$^{-1}$ S$^{-1}$) [7], a short hole diffusion length (2-4 nm) [8], slow surface reaction kinetics, and electron-hole recombination in the bulk and at the semiconductor/liquid junction [9]. The slow oxygen evolution reaction (OER) kinetics and the existence of surface trap sites cause the experimental solar-to-hydrogen efficiency to be less than the theoretical value and significantly restrict the practical application of $Fe_2O_3$ in solar energy conversion [10,11]. For overcoming these drawbacks and improving the PEC performance of $Fe_2O_3$, heterojunction construction [12], element doping [13], and $O_2$ defect creation [14] have been utilized. Generally, the high positive onset potential of the $Fe_2O_3$ electrode is one of the main issues preventing good PEC performance. For reducing the onset potential, surface modification is an effective strategy to improve the OER kinetics by reducing the amount of surface trap sites and has attracted considerable attention [15,16]. Additionally, surface etching [17] was demonstrated to be effective for reducing the degree of surface recombination and accelerating the OER kinetics [18]. Li et al. reported that simple acid-treated hematite nanowire photoanodes had significantly reduced surface electron-hole recombination losses due to their improved PEC performance. They reported that the significantly reduced surface electron-hole recombination losses for the acid-treated hematite were due to the larger number of trapped photoelectrons extracted to the external circuit [19]. Zou et al. applied the HCl acid solution corrosion method to $Ti^{4+}$ doped $Fe_2O_3$ and confirmed that the treated $Ti^{4+}$-doped $Fe_2O_3$ sample displayed a 100-mV cathodic shift in the photocurrent onset potential [17]. In addition to acid treatments, loading of water oxidation cocatalysts, including $IrO_2$, $RuO_2$, $Co_3O_4$, NiOOH, and $NiO_x$, on the surface of nanostructured electrodes has been used to speed up the photogenerated holes reaching the semiconductor/liquid junction [20,21]. Hu et al. obtained a 150-mV cathodic shift of the

†To whom correspondence should be addressed.
E-mail: mahadeomahadik@gmail.com, jangjs75@jbnu.ac.kr
Copyright by The Korean Institute of Chemical Engineers.

onset potential via surface adsorption of $F^-$ ions on an $Fe_2O_3$ electrode [22]. Additionally, our group reported an improvement in the PEC performance of a tetravalent ion-doped $Fe_2O_3$ nanorod photoelectrode due to $CoO_x$ cocatalyst modification [23]. Although various cocatalysts have been utilized for improving the PEC performance of $Fe_2O_3$, most of the studies involved single-component cocatalysts, whose co-catalytic effects were constrained to the chemical, physical, and electronic properties of the material [24]. Thus, reducing all possible recombination pathways simultaneously is imperative for further improving the PEC water-splitting performance of hematite at a low onset potential. There are no reported studies in which the problems of the large overpotential and low efficiency of initial charge separation and electron transfer in $Fe_2O_3$ NC photoanodes were solved by removing the surface states through synergistic acid treatment and co-catalyst loading.

In this study, we demonstrated the synergistic effects of nitric acid treatment and $CoO_x$ surface adsorption on the electronic properties, surface charge transfer efficiency, and PEC performance of Zr-doped hematite NC photoanodes. Acid treatment is beneficial for functionalizing the surface for effective $CoO_x$ adsorption and charge transport. Compared with bare Zr-$Fe_2O_3$ NC photoanodes, $CoO_x$-encapsulated acid-treated Zr-$Fe_2O_3$ NC exhibited a higher photocurrent density (1.83 mA/cm$^2$ at 1.23 V (vs. reversible hydrogen electrode (RHE)) along with a 200-mV cathodic shift in the photocurrent onset. The enhanced PEC performance was explained as follows: the assimilation of surface-adsorbed $CoO_x$ and nitric acid increased the active surface area, optimum light absorption, and surface charge-transfer rate at the photoelectrode/electrolyte junctions. Furthermore, the optimum $CoO_x$-encapsulated acid-treated Zr-$Fe_2O_3$ NC was used as a photoanode in PEC water oxidation. Additionally, we proposed the charge-transfer mechanism between the acid-treated photoelectrode surface and $CoO_x$ during PEC water splitting. The present strategy provides new insights into the roles of the acid treatment and metal-oxide adsorption for effective solar water splitting.

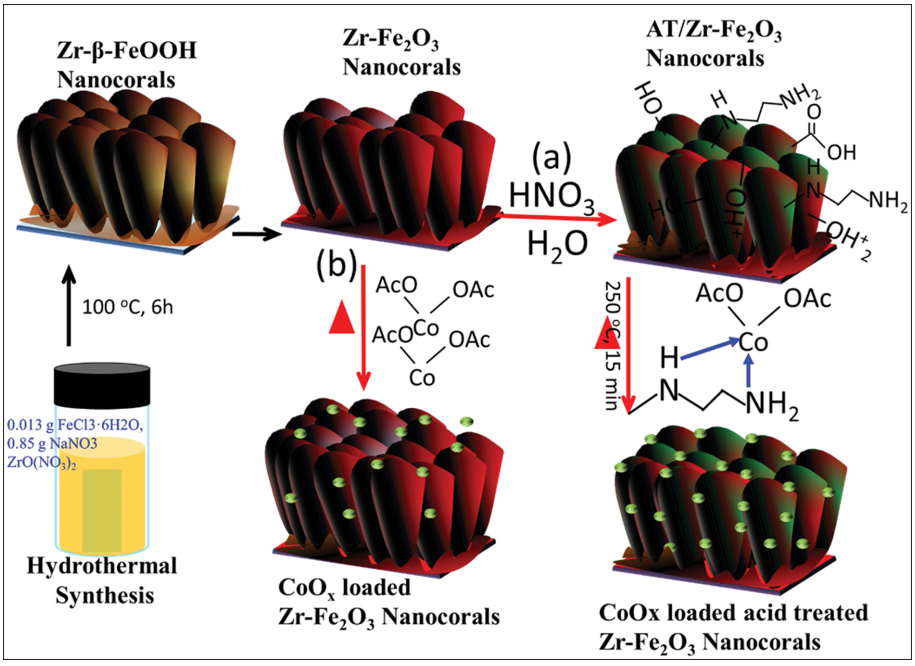
## EXPERIMENTAL SECTION

### 1. Reagents and Chemicals

Fluorine-doped tin oxide (FTO) glass (10-15 Ω/cm), acetone (99.5%, Samchun), ethanol (94.5%, Samchun), deionized water (5 μs/cm$^2$, RO), $FeCl_3{\cdot}6H_2O$ (97%, Sigma-Aldrich), $NaNO_3$ (≥99%, Sigma-Aldrich), HCl (37%, Sigma-Aldrich), a zirconyl nitrate solution (35 wt% ≥99% trace metals basis, Sigma-Aldrich), and nitric acid ($HNO_3$, 69%, Junsei) were used.

### 2. Synthesis of Hematite Films and Surface Treatment

Bare-$Fe_2O_3$ and Zr-doped $Fe_2O_3$ photoanodes were synthesized using the method described in our previous report [25]. In a typical procedure, *in situ* Zr-doped hematite was synthesized by adding 1 mL of an Zr($NO_3$)-ethanol solution (4.1336 μl/10 mL), which was added to the hydrothermal precursor solution as reported previously for Sn *in situ* doping [26]. The precursor solution was prepared in 10 mL of deionized water (5 μs/cm, RO) using 0.013 g of $FeCl_3{\cdot}6H_2O$ and 0.85 g of $NaNO_3$. The pH of the solution was adjusted to 1.5 using HCl [27]. A 4.1336 μL/10 mL zirconyl nitrate-ethanol solution was prepared separately and 1 mL of the zirconyl nitrate-ethanol solution was added to the hydrothermal precursor solution. The glass vials containing the synthesis solution and four FTO substrates were heated in an electric oven at 100 °C for 6 h. After cooling, the Zr-doped FeOOH films deposited on the FTO were washed several times with distilled water, dried via $N_2$ gas purging, and quenched at 800 °C for 11 min. Further, the samples were termed as Zr-$Fe_2O_3$ NC photoanodes. Acid-treated Zr-$Fe_2O_3$ photoanodes were subsequently obtained using 0.1 M nitric acid




**Scheme 1. Schematics of the $CoO_x$ surface encapsulation over (a) with and (b) without $HNO_3$ treated Zr-$Fe_2O_3$ NC photoanodes.**

(69%). The as-prepared Zr-$Fe_2O_3$ films were immersed in 0.1 M nitric acid (69%) for 3, 6, 12 and 18 h and then rinsed thoroughly with distilled water and dried gently with $N_2$ gas. The surface acid-treated Zr-$Fe_2O_3$ samples were denoted as AT-3/Zr-$Fe_2O_3$, AT-6/Zr-$Fe_2O_3$, AT-12/Zr-$Fe_2O_3$, and AT-18/Zr-$Fe_2O_3$, respectively.

**3. Preparation of $CoO_x$-encapsulated Acid-treated Hematite Films**

To prepare the $CoO_x$ overlayer, 1 mM $Co(OAc)_2$ solutions in ethanol were spin-coated (2,500 rpm for 25 s) onto the acid-treated Zr-$Fe_2O_3$ photoanodes, followed by heat treatment at 250 °C for 15 min. The $CoO_x$ encapsulated 3, 6,12 and 18 h surface acid-treated Zr-$Fe_2O_3$ prepared via the spin-coating method was denoted as a $CoO_x$/AT-3/Zr-$Fe_2O_3$, $CoO_x$/AT-6/Zr-$Fe_2O_3$ $CoO_x$/AT-12/Zr-$Fe_2O_3$ and $CoO_x$/AT-18/Zr-$Fe_2O_3$ photoanodes. To confirm the effect of the acid treatment, the $CoO_x$/Zr-$Fe_2O_3$ NC array photoanodes without acid treatment were prepared under similar conditions. The synthesis of the $CoO_x$ surface-modified AT-12/Zr-$Fe_2O_3$ NC array photoanodes is described in Scheme 1.

**4. Characterization**

X-ray diffraction (XRD) patterns of the prepared Zr-$Fe_2O_3$ photoelectrodes were obtained using an XPERT-PRO diffractometer with a CuK$\alpha$ radiation source ($K_{\alpha1}$ wavelength=1.540598 Å and $K_{\alpha2}$ wavelength=1.544426 Å). The surface and cross-sectional images of the photoanodes were analyzed using field-emission scanning electron microscopy (FESEM, JEM-2010, SUPRA40VP, Germany). A Shimadzu ultraviolet-visible (UV-vis) spectrophotometer (UV-2600) was used to collect the UV-vis-diffuse reflectance (UV-vis-DRS) spectra of the Zr-$Fe_2O_3$ photoanodes. X-ray photoelectron spectroscopy (XPS) was performed using a PHI Quantera II spectrometer with a monochromatic AlK$\alpha$ X-ray source (h$\nu$=1,486.6 eV, 25 W, and 15 kV). A time-resolved photoluminescence (TRPL) study was performed using a confocal microscope (MicroTime-200, Picoquant, Germany). A single-mode pulsed diode laser with a power of 0.5 mW, pulse width of ~30 ps, and repetition rate of 20 MHz (LDH-P-C-470, Picoquant, Germany) was used as the excitation source. The time-correlated single-photon counting technique was used to count the emission photons. TRPL images consisting of 200×200 pixels were obtained using the time-tagged time-resolved data-acquisition method with an acquisition time of 2 ms per pixel. Exponential fitting for the PL decays with a temporal resolution of 8 ps, which were extracted from the TRPL images, was performed via iterative least-squares deconvolution fitting using the software Symphotime-64 (Ver. 2.2) with the exponential decay model, as follows [28]:

$$I(t)=\Sigma A_i e^{-t/\tau_i}, \quad (1)$$

where I (t) represents the time-dependent photoluminescence (PL) intensity, $\tau$ represents the PL lifetime, i=2, and A represents the amplitude. The average lifetime $<\tau>$ is defined as follows [29]:

$$<\tau>=\Sigma A_i \tau_i^2/\Sigma A_i \tau_i. \quad (2)$$

**5. PEC Measurements**

PEC measurements were performed with a specially designed three-armed cell using an Ivium CompactStat potentiostat, as well as a solar simulator with standard solar light (AM 1.5G, 100 mW $cm^{-2}$). The Zr-$Fe_2O_3$-based electrodes, a Pt wire, and Hg/HgO were used as the working, counter, and reference electrodes, respectively. A 1.0 M NaOH aqueous solution (pH of 13.6) was used as the electrolyte. During the PEC measurements, all the electrodes were front-side illuminated, and the area of the working electrode was fixed at 1.0 $cm^2$. The measured potentials were converted to the RHE via the Nernst equation [26,27]:

$$E_{vs.\ RHE}=E_{vs.\ Hg/HgO}+0.059pH+E^o_{Hg/HgO};\ (E^o_{Hg/HgO}=0.095\ V \text{ at } 25\ ^oC). \quad (3)$$

The current density versus potential (*J*-V) curves were measured with a scan rate of 50 mV $s^{-1}$. Electrochemical impedance spectroscopy (EIS) analyses were performed over the frequency range of 3,000 kHz to 0.5 Hz under illumination and applied potential of 1.23 V vs. RHE. Intensity-modulated photocurrent spectroscopy (IMPS) was carried out using the same three-electrode PEC cell configuration, with a green light-emitting diode (peak wavelength of 520 nm) driven by a frequency-response analyzer. The frequency was swept from 10 kHz down to 0.1 Hz with 10% light-intensity modulation.

The surface charge-separation efficiency ($\eta_{surface}$) and bulk charge-separation efficiency ($\eta_{bulk}$) of the Zr-$Fe_2O_3$ and AT-12/Zr-$Fe_2O_3$ photoanodes were measured by adding a hole scavenger (0.5 M $H_2O_2$) to a 1 M NaOH electrolyte. The $\eta_{bulk}$ was calculated using the following equation [30]:

$$J_{H_2O}=J_{abs}\times(\eta_{bulk})\times(\eta_{surface}), \quad (4)$$

where $J_{H_2O}$ represents the experimental photocurrent density, and $J_{abs}$=100% represents the absorbed photon-to-current efficiency. The oxidation kinetics of the system are rapid after the addition of 0.5 M $H_2O_2$ to the NaOH electrolyte, which reduces the surface recombination without degrading the charge separation in the bulk; therefore, $\eta_{surface}$ can be considered as 100%. Thus, $\eta_{surface}$ and $\eta_{bulk}$ can be calculated using the following equations [26]:

$$\eta_{bulk}=J_{H_2O_2}/J_{abs} \quad (5)$$

$$\eta_{surface}=J_{H_2O}/J_{H_2O_2}, \quad (6)$$

where $J_{H_2O_2}$ represents the photocurrent density in the presence of $H_2O_2$.

PEC water splitting was conducted in an air tight three-electrode PEC reactor. The optimum $CoO_x$/AT-Zr-$Fe_2O_3$ NC electrode, a Pt wire, and Hg/HgO were used as the working, counter, and reference electrodes, respectively. 1 M NaOH was used as the electrolyte for the PEC water-splitting experiments. The photoanodes was illuminated with solar simulator light (AM 1.5G, 100 mW $cm^{-2}$). The evolved $O_2$ and $H_2$ gases generated during the PEC water splitting were measured using a gas chromatography (GC) system equipped with a thermal conductivity detector (Agilent 7820, USA) with a 5-Å molecular sieve column [31].

## RESULTS AND DISCUSSION

**1. Characterization of Acid-treated $Fe_2O_3$ Photoanode**

To examine the surface morphology of the *in situ* Zr-doped $Fe_2O_3$ photoanodes before and after the acid treatment, top and cross-sectional FESEM images were obtained, as shown in Fig. 1. Both the optimum bare (Zr-$Fe_2O_3$) and acid-treated Zr-doped hematite

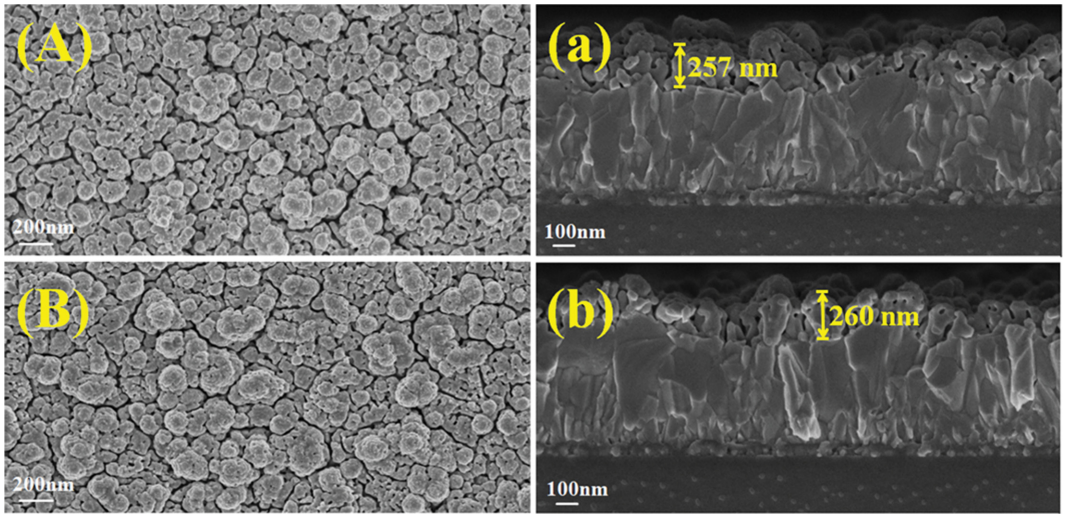



**Fig. 1. (A), (B) Top-view (left) and (a), (b) cross-sectional FESEM images (right) of optimum Zr-$Fe_2O_3$ photoanodes before and after surface acid treatment.**

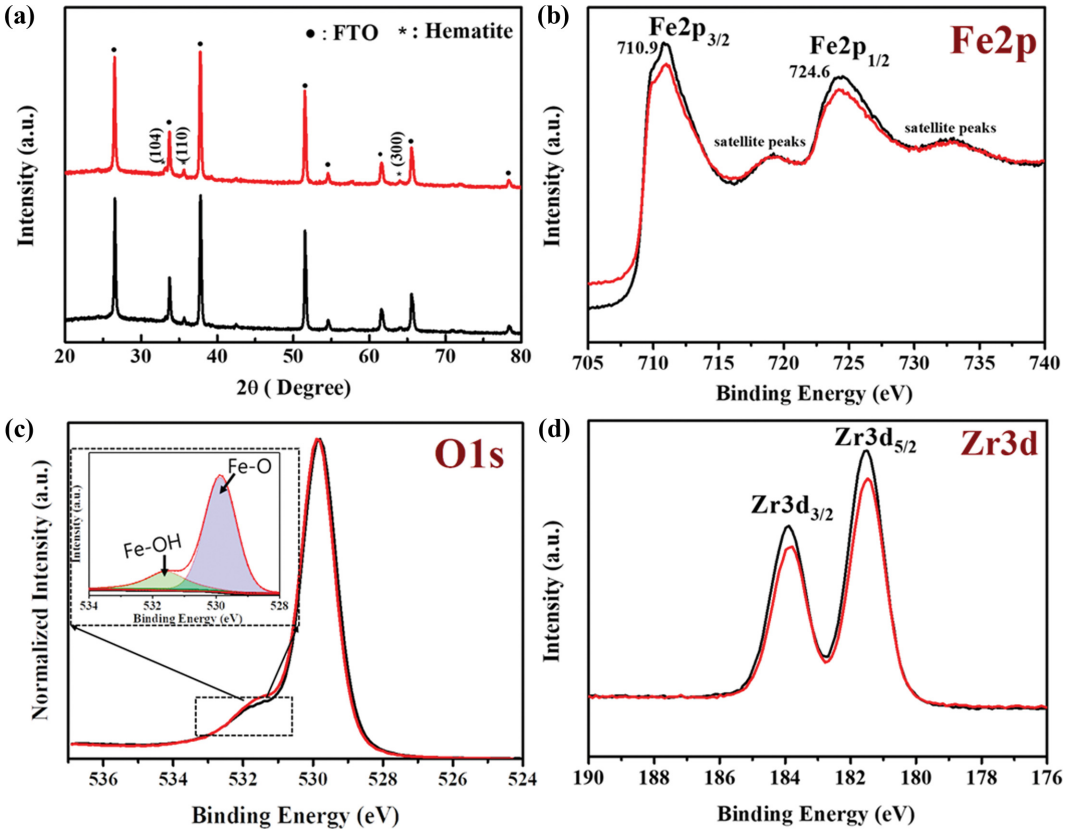



**Fig. 2. (a) X-ray diffraction patterns and (b)-(d) high resolution XPS spectra of Fe, O and Zr for bare Zr-$Fe_2O_3$ (black) and AT-12/Zr-$Fe_2O_3$ (red) photoanodes.**

photoanodes exhibited vertically aligned NCs on the FTO substrates. The NCs had widths of 35-58 nm and lengths of ~260 nm [27]. As shown in Figs. 1(a) and (b), the acid treatment did not significantly affect the morphology of the Zr-doped hematite NCs.

Fig. 2(a) shows the XRD patterns of the bare and acid-treated Zr-$Fe_2O_3$ NC photoanodes. The XRD peaks of the acid-treated Zr-doped hematite photoanodes exhibited similar features to those of the untreated Zr-doped hematite films prepared via *in situ* doping. The characteristic diffraction peaks of both the photoanodes were indexed to the hematite phase ($\alpha$-$Fe_2O_3$, denoted as "*," JCPDS 33-0664) and the substrate FTO phase ($SnO_2$, denoted as "•," JCPDS 41-1445). No diffraction peaks of $ZrO_2$ or other impurity phases

were observed for any of the samples. XPS is a sensitive surface spectroscopy technique to confirm the surface composition of the Zr-$Fe_2O_3$ NCs after acid treatment. The XPS survey scan spectra of the bare and acid-treated Zr-$Fe_2O_3$ NC photoanodes clearly exhibited peaks at binding energies (BE's) of 530 and 711 eV, which are the characteristic peaks of O 1s and Fe 2p, respectively, suggesting the presence of O and Fe (Fig. S1). Fig. 2(b) shows the high-resolution XPS Fe2p spectra of both untreated (bare) and acid-treated Zr-$Fe_2O_3$ NC photoanodes. The Fe $2p_{1/2}$ peak and Fe $2p_{3/2}$ peak at BEs of 724.6 and 711.3 eV, respectively, correspond to the $Fe^{3+}$ in $Fe_2O_3$ [19,32]. Regarding the satellite peak centered at 718 eV, the acid-treated photoanodes exhibited slightly a higher peak than the bare Zr-$Fe_2O_3$ NC photoanodes, indicating the formation of $Fe^{2+}$ sites on the surface during the acid treatment [33,19]. In addition to Fe2p, the acid-treated Zr-doped hematite photoanodes

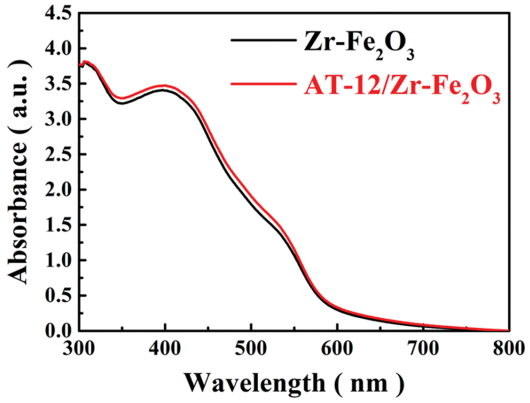



**Fig. 3. UV-vis absorbance spectra of Zr-$Fe_2O_3$ and AT-12/Zr-$Fe_2O_3$ photoanodes.**

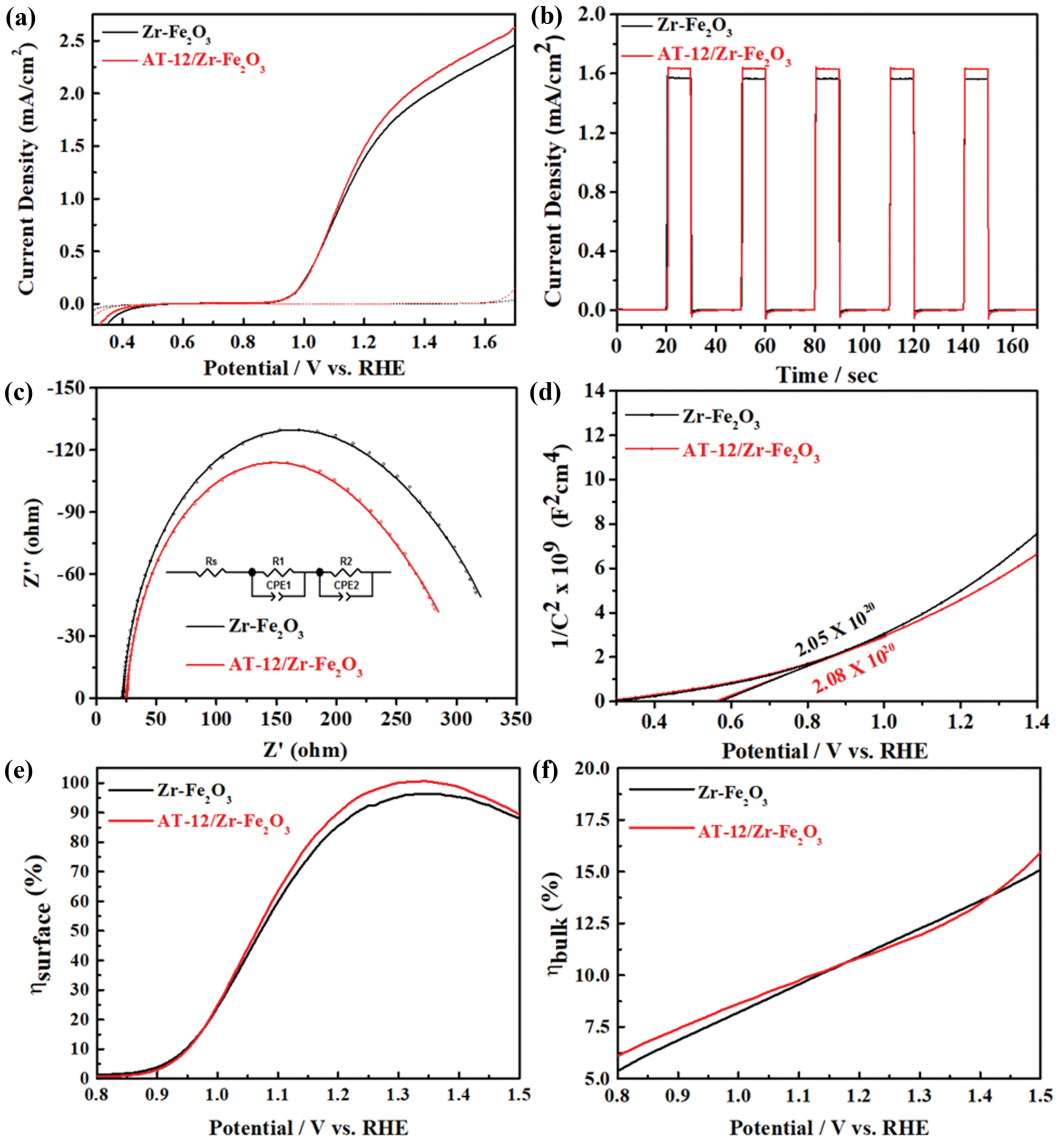



**Fig. 4. (a) Photocurrent-potential (J-V) curves and (b) transient photocurrent responses under chopped one sun illumination condition, (c) EIS Nyquist plots at 1.23 V vs. RHE under 1 sun standard illumination conditions, The inset shows the equivalent electric circuit used to fit the EIS plots, (d) Mott Schottky, ((e) and (f)) surface charge separation efficiency ($\eta_{surface}$) and bulk ($\eta_{bulk}$) charge separation efficiency for bare Zr-$Fe_2O_3$ NC and acid treated Zr-$Fe_2O_3$ NC photoanodes.**

exhibited a slight shoulder peak at 532.3 eV than the O 1s peak of the untreated Zr-$Fe_2O_3$ NC photoanode (Fig. 2(c)). This was attributed to the O-Fe(OH) of FeOOH. However, as the FeOOH content was low, iron hydroxide was not detected in the XRD analysis [34]. The XPS spectra of Zr 3d (Fig. 2(d)) exhibited two Zr peaks at BEs of 181.40 and 183.3 eV for both the bare and acid-treated Zr-$Fe_2O_3$ NC photoanodes, confirming that the Zr was in the 4+ state [35]. Furthermore, the UV-vis-DRS absorbance spectra of the Zr-$Fe_2O_3$ and AT-12/Zr-$Fe_2O_3$ were measured (Fig. 3). AT-12/Zr-$Fe_2O_3$ exhibited a minor difference in the absorbance, but the bandgap did not differ significantly from those of the other samples.

To study the effect of the acid treatment on the PEC performance of the Zr-doped $Fe_2O_3$ NCs, the *J-V* curves of the hematite samples with and without acid treatment were measured and are shown in Fig. 4(a). The optimized AT-12/Zr-$Fe_2O_3$ photoanodes exhibited slightly increased photocurrent density and no shift in onset potential as the untreated sample (Zr-$Fe_2O_3$ photoanode). Also, Fig. S2 shows the effect of acid treatment time on the photocurrent of the Zr-$Fe_2O_3$ nanocoral photoanodes. Further, the photoresponse of the Zr-$Fe_2O_3$ photoelectrode was studied using transient photocurrent density measurements under chopped light illumination in a 1 M NaOH electrolyte at 1.23 V *vs.* RHE (Fig. 4(b)). Both the Zr-$Fe_2O_3$ and acid-treated Zr-$Fe_2O_3$ photoelectrodes exhibited quick and reproducible photoresponse under the chopped illumination, suggesting effective charge transport in the photoanodes. To further study the charge-transfer kinetics and interfacial property after acid treatment of Zr-$Fe_2O_3$ NC, EIS was performed under 1-sun illumination at 1.23 V *vs.* RHE. Fig. 4(c) shows the Nyquist plots of the Zr-$Fe_2O_3$ and AT-12/Zr-$Fe_2O_3$ photoanodes in a 1 M NaOH electrolyte under visible-light illumination at 1.23 V *vs.* RHE. The inset shows the equivalent electric circuit used to fit the EIS plots. The equivalent circuit consists of the series resistance ($R_s$), which includes mainly the sheet resistance of the FTO and resistance of external wires; $R_1$, $R_2$ and $CPE_1$, $CPE_2$ are the charge-transfer resistances and double-layer capacitances at the FTO/Zr-$Fe_2O_3$ and electrode/electrolyte interfaces, respectively [36,37]. As shown in Fig. 4(c), in the low-frequency region, the radius of the AT-12/Zr-$Fe_2O_3$ photoanode EIS curve became smaller than that for the untreated Zr-$Fe_2O_3$, indicating an increased charge-transfer rate at the electrode/electrolyte interface after the acid treatment. Table 1 clearly shows that in addition to $R_1$, $R_2$ decreased from 205 to 189 Ω and 131 to 74 Ω for the AT-12/Zr-$Fe_2O_3$ and Zr-$Fe_2O_3$ photoanodes. Cao et al. synthesized HCL-treated $Fe_2O_3$ and reported that the improved charge-transfer rate at the electrode/electrolyte interface originated from the suppression of the back reaction [17]. Mott-Schottky plots of the Zr-$Fe_2O_3$ and acid-treated Zr-$Fe_2O_3$ photoelectrode were obtained from 0.3 to 1.7 V vs. RHE at a frequency of 100 Hz in the dark, as shown in Fig. 4(d). The donor density ($N_d$) was estimated using the equation given below [38,39]:

$$N_d=(2/e_0\varepsilon\varepsilon_0)\ [d(1/C^2)dV]^{-1} \quad (7)$$

where, $e_0$ and $\varepsilon$ represents the electron charge ($1.602\times10^{-19}$ C) and dielectric constant of hematite (80), whereas the $\varepsilon_0$ and C represents the permittivity of vacuum ($8.854\times10^{-12}$ F $m^{-1}$) and capacitance derived from the electrochemical impedance obtained at each potential (V). Fig. 4(d) shows that the untreated and acid-treated Zr-$Fe_2O_3$ NC photoanode exhibit nearly same donor density.

To confirm the charge-separation effect due to the acid treatment of Zr-$Fe_2O_3$, the surface and bulk charge-separation efficiencies were calculated according to the photo-oxidation of $H_2O_2$ as a hole scavenger. As shown in Fig. 4(e) and (f), the $\eta_{bulk}$ values of bare Zr-$Fe_2O_3$ NC and AT-12/Zr-$Fe_2O_3$ NC photoanodes were 11.3% and 11.2% at 1.23 V vs. RHE, and the $\eta_{surface}$ values of the AT-12/Zr-$Fe_2O_3$ NC photoanode were calculated to be 94.8% at 1.23 V vs. RHE (Fig. 4(f)), which were slightly higher than those of the Zr-$Fe_2O_3$ NC (90.1%) photoanodes. Although the bulk efficiency was identical for the Zr-$Fe_2O_3$ and acid-treated Zr-$Fe_2O_3$ photoelectrodes, enhanced surface efficiency led to suppressed surface recombination. These results clearly suggest that acid treatment can modify the surface of Zr-$Fe_2O_3$ NCs, which is helpful for assembling an effective photoanode for rapid water oxidation. Furthermore, the electron transport time ($\tau_d$), i.e., the average time interval from the generation to the collection of electrons at the rear FTO, was calculated using the IMPS spectra of the Zr-$Fe_2O_3$ and acid-treated Zr-$Fe_2O_3$ photoanodes (Fig. S3). Here, the following equation was used: $\tau_d=1/(2\pi f_{min})$, where $f_{min}$ represents the frequency of the minimum point in the IMPS semicircle [40]. The electron transport times ($\tau_d$) for the Zr-$Fe_2O_3$ and acid-treated Zr-$Fe_2O_3$ photoelectrodes (0.28 and 0.26 ms, respectively) indicate that the acid treatment slightly affected the bulk resistance of the carrier recombination. This agrees well with the EIS analysis [41].

**2. Characterization of Co-encapsulated Acid-treated $Fe_2O_3$ ($CoO_x$/AT-12/Zr-$Fe_2O_3$) Photoanodes**

To investigate the effect of the acid treatment on the Zr-$Fe_2O_3$ during PEC water oxidation, the photocurrent density of $CoO_x$/AT-12/Zr-$Fe_2O_3$ was measured and compared with that of the $CoO_x$/Zr-$Fe_2O_3$ photoanodes under standard one sun illumination. As shown in Fig. 5(a), the photocurrent density of $CoO_x$/AT-12/Zr-$Fe_2O_3$ was 1.8 mA/$cm^2$ at 1.23 V *vs.* RHE (surface modification with 1 mM $Co(OAc)_2$ solution), which was enhanced by approximately 200 μA·$cm^{-2}$ compared with that of the $CoO_x$/Zr-$Fe_2O_3$ NC photoanode. Furthermore, the onset potential of $CoO_x$/AT-12/Zr-$Fe_2O_3$ was shifted by 200 mV in the negative direction compared with that of the bare Zr-$Fe_2O_3$ NC photoanode. Thus, the synergy between the acid treatment and $CoO_x$ surface modification significantly affected the water-oxidation performance of the optimum $CoO_x$/AT-12/Zr-$Fe_2O_3$ photoanode. A major reason for the improved photocurrent for the $CoO_x$/AT-12/Zr-$Fe_2O_3$ photoanode

**Table 1. EIS fitting parameters obtained by fitting the Nyquist plots of Zr-$Fe_2O_3$ and AT-12/Zr-$Fe_2O_3$ using the equivalent circuit**

| Samples | $R_S$ (Ω) | $R_1$ (Ω) | $CPE_1$ (μF) | $R_2$ (Ω) | $CPE_2$ (μF) |
|---|---|---|---|---|---|
| Zr-$Fe_2O_3$ | 22 | 205 | 24 | 131 | 297 |
| AT-12/Zr-$Fe_2O_3$ | 25 | 189 | 22 | 74 | 1,130 |

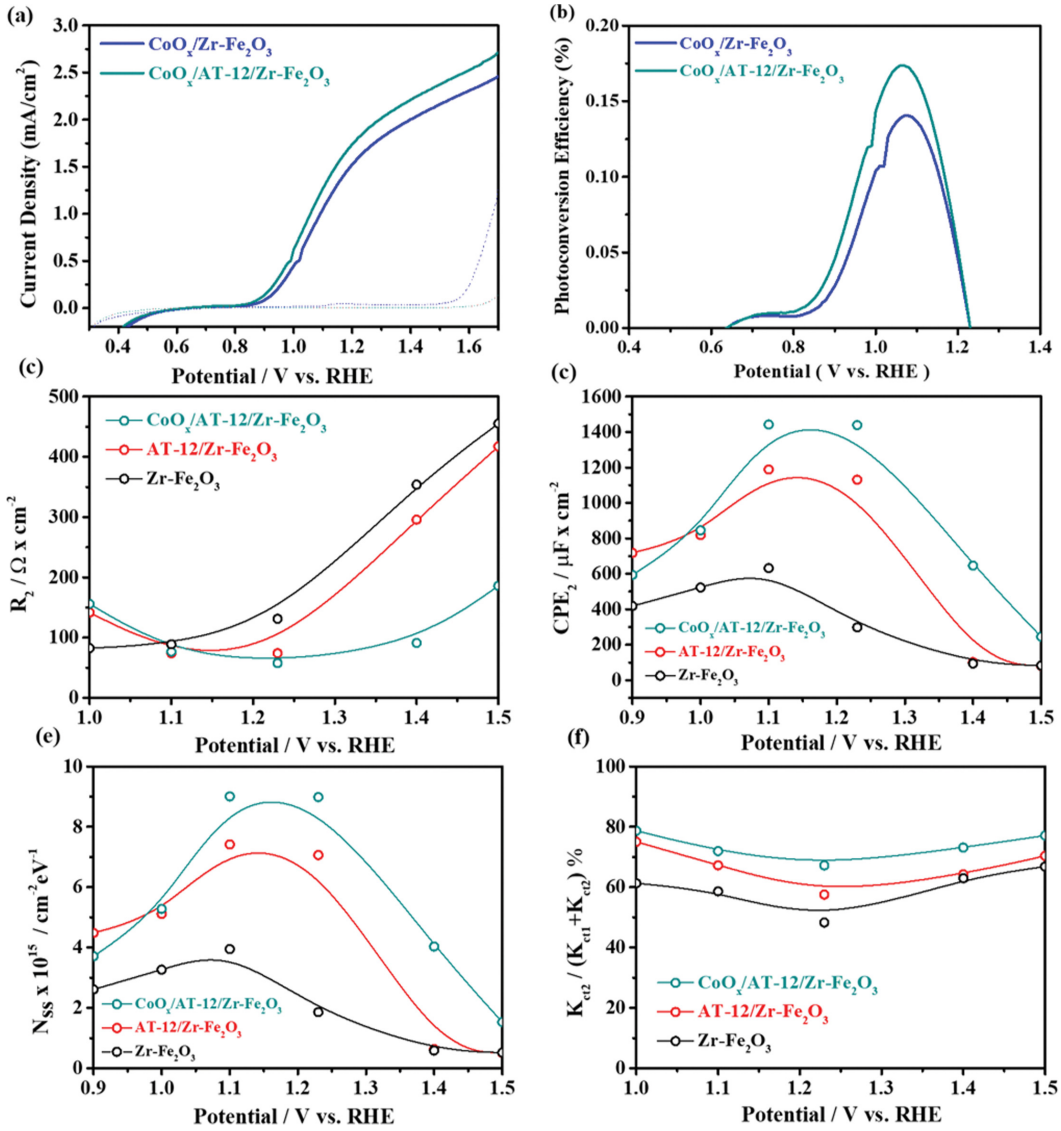



**Fig. 5. (a) J-V curves; (b) applied bias photon-to-current conversion efficiency of $CoO_x$/Zr-$Fe_2O_3$ (blue) and $CoO_x$/AT-12/Zr-$Fe_2O_3$ (dark cyan) photoanodes in a 1 M NaOH electrolyte at 1.23 V vs. RHE, (c) resistance ($R_2$) and (d) associated capacitance ($CPE_2$) with the charge transfer at/from surface states with different applied potential obtained upon illumination: 100 mW cm$^{-2}$, AM 1.5G, (e) surface state density ($N_{SS}$), (f) ratio of the charge transfer rate constant ($k_{ct2}$) and the sum of the charge transfer and trapping ($k_{ct2}$+$k_{ct1}$) rate constants as a function of applied potential.**

was that the presence of $OH^-$ on the acid-treated Zr-$Fe_2O_3$ allowed the adsorption of more $CoO_x$ on the surface. Additionally, the $OH^-$ attracted the photogenerated holes in the Zr-$Fe_2O_3$ NC and was simultaneously transferred to the $CoO_x$ present on the surface [42]. Furthermore, the ~200-mV cathodic shift of the onset potential indicated an important synergistic role of the acid treatment and $CoO_x$ film in the $CoO_x$/AT-Zr-$Fe_2O_3$ NC system. To examine the effect of the acid treatment on the photoconversion efficiencies of $CoO_x$/Zr-$Fe_2O_3$ NC and $CoO_x$/AT-Zr-$Fe_2O_3$ NC, the equation reported by Mahadik et al. was used [43]. As shown in Fig. 5(b), the photoconversion efficiency of $CoO_x$/AT-12/Zr-$Fe_2O_3$ NC (0.14%) at 1.0 V *vs.* Hg/HgO under 1-sun illumination was higher than that of $CoO_x$/Zr-$Fe_2O_3$ NC (0.1%), which was attributed to the improvement of the $CoO_x$ adsorption and reduction of the surface electron-hole recombination due to the acid treatment. The catalytic activity of photoanodes is strongly dependent on the appearance of the surface states (SS) at the electrode-electrolyte interface [44]. The presence of the surface states (SS) acting as electron-hole recombination centers and also depending on their certain kinetics SS can be a beneficial influence on water oxidation, promoting electron transfer across the interface [45]. It is well known that doped semiconductors with sufficient thickness photoelectrode materials have two types of capacitance (bulk capacitance, $C_{bulk}$, and chemical capacitance, $C_{ss}$), where $C_{bulk}$ is the combination of the two dielectrics in origin capacitances such as space charge capacitance, $C_{sc}$ defined by the Mott-Schottky (MS) and the series connection of $C_H$ and another is $C_{ss}$, which is chemical capacitance in the same system [46]. Therefore, to assess the role of sur-

face states existing at the hematite/electrolyte interface on the water-splitting process, electrochemical impedance spectroscopy under illumination was measured at different applied potential. The equivalent circuits were used to fit the EIS (inset of Fig. 4(c)), and the values of fitted parameters used to determine the SS and charge transfer kinetics. In the present study, surface states affecting the charge transfer of holes to the donor species in solution are described by $R_2$, and the direct charge transfer from the semiconductor bands is $R_1$ [46,47]. Fig. 5(c), (d) shows as the applied potential increases, the $CPE_2$ value peaks with the decrease in $R_2$, resulting from the hole-transfer step leading to water oxidation takes place predominantly from surface trapped holes (dominated by SS) [48]. Fig. 5(d) clearly shows Zr-$Fe_2O_3$ photoanodes exhibit the increase of $CPE_2$ up to 1.1 V vs RHE with a simultaneous decrease of $R_2$ with the applied bias increasing. Advancement is observed in $CPE_2$ after the acid treatment in AT-12/Zr-$Fe_2O_3$ photoanodes signifying the formation of additional surface states on the photoanode. Furthermore, the increased $CPE_2$ values of the $CoO_x$/AT-12/Zr-$Fe_2O_3$ photoanodes indicate that the synergistic effect of acid treatment and $CoO_x$ contributes to accelerating the hole trapping. Furthermore, capacitance ($CPE_2$) used to estimate the density of surface states (DOSS) was as follows:

$$Nss(E)=CPE_2(E)/q \quad (8)$$

where, Nss (E) is the DOSS ($cm^{-2}$ $eV^{-1}$) as a function of the applied potential and q is the electron charge ($1.602\times10^{-19}$ C) [47]. Fig. 5(e) shows the combined comparison of the Nss with respect to the applied potential. Due to low electrical conductivity (higher values of $R_1$ and $R_2$), the Zr-$Fe_2O_3$ NC and AT-12/Zr-$Fe_2O_3$ NC photoanodes demonstrate poor PEC performance. On the other hand, with the increase in applied potential, the $CPE_1$ ($C_{bulk}$) decreases (Fig. S4(b)), whereas the $CPE_2$ increases (Fig. 5(d)), implying a larger percentage of charge located on SS in $CoO_x$/AT-12/Zr-$Fe_2O_3$ NC photoanode enables a higher photocurrent [49]. The charge transfer efficiency at the photoelectrode/electrolyte interface is examined by using the following formula [50]:

$$\text{Transferefficiency (\%)}=k_{ct1}/(k_{ct1}+k_{ct2})=R_1/(R_2+R_1) \quad (9)$$

where, $k_{ct1}$ and $k_{ct2}$ are the charge transfer and trapping rate constants, respectively, and $R_1$ and $R_2$ are the corresponding resistances (Fig. S4(a) and Fig. 5(c)). As shown in Fig. 5(f), the optimized $CoO_x$/AT-12/Zr-$Fe_2O_3$ NC photoanodes exhibit over 67% of the hole transferefficiency at electrode/electrolyte interface at 1.23 V vs. RHE, which is about 20% higher than that of the Zr-$Fe_2O_3$ NC photoanodes. These results are in good agreement with the photocurrent density (Fig. 5(a)). The photoresponse of the $CoO_x$/Zr-$Fe_2O_3$ NC and $CoO_x$/AT-12/Zr-$Fe_2O_3$ NC photoelectrode was studied using transient photocurrent density measurements under chopped light illumination in a 1 M NaOH electrolyte at 1.23 V vs. RHE (Fig. S4(c)). Both the $CoO_x$/Zr-$Fe_2O_3$ and acid-treated $CoO_x$/Zr-$Fe_2O_3$ photoelectrodes exhibited fast photoresponse under chopped illumination, indicating the effective charge transport in the photoanodes. The PEC stability of $CoO_x$/Zr-$Fe_2O_3$ (blue) and $CoO_x$/AT-12/Zr-$Fe_2O_3$ (dark cyan) photoanodes were tested for 3,600 s under one sun illumination in 1 M NaOH at 1.23 V *vs.* RHE, as presented in Fig. S4(d). It can be estimated that both $CoO_x$/Zr-$Fe_2O_3$ and $CoO_x$/AT-12/Zr-$Fe_2O_3$ photoanodes show nearly no significant change while PEC water splitting, which promises the good stability of these two photoanodes. The incident photon-to-current conversion efficiency (IPCE) was calculated using the equation reported by Jeong et al. [27]. As shown in the figure, IPCE exhibits generation of the photocurrent starting at 590 nm and reaches peak values in the short-wavelength region at 400 nm. Further, the integrated current density was calculated from the IPCE values photoanodes at 1.23 V vs RHE. The synergistic effects of the $CoO_x$ adsorption and acid treatment improved the IPCE of $CoO_x$/AT-Zr-$Fe_2O_3$ NC (44.6%) compared with the $CoO_x$/Zr-$Fe_2O_3$ NC (41.9%) and photoanodes (Fig. S5). The IPCE improvement was due to the reduced electron-hole recombination and transfer of photogenerated holes for PEC water oxidation with little efficiency loss [51]. However, compared with Zr-$Fe_2O_3$ and AT-12/Zr-$Fe_2O_3$, the UV-vis-DRS absorption of $CoO_x$/AT-12/Zr-$Fe_2O_3$ was slightly higher, as shown in Fig. S6. Thus, AT-12/Zr-$Fe_2O_3$ exhibited a slight variation in absorbance, but the optical bandgap was not significantly different from that of the other samples. Top-view FESEM images of the $CoO_x$/Zr-$Fe_2O_3$ NC and $CoO_x$/AT-12/Zr-$Fe_2O_3$ NC photoanodes revealed no significant changes in the morphologies of the photoanodes (Fig. S7). To find the presence of the Cobalt, XPS analyses of $CoO_x$/AT-12/Zr-$Fe_2O_3$ photoanodes were carried out. Fig. S8(a) shows the survey scan of $CoO_x$/AT-12/Zr-$Fe_2O_3$ NC photoanode which clearly indicates the presence of the Fe, O, and Zr elements. The C 1s peak is due to the widespread presence of carbon in the environment. High resolution Co2p XPS spectra shown in Fig. S8(b) could be best fitted by four peaks at 779.1, 780.5, 781.2 and 797 eV, respectively. These Co2p peaks are associated with $Co^{3+}$ ($Co_2O_3$), $Co^{2+}$ (CoO), $Co^{3+}$ ($Co_2O_3$) and $Co^{2+}$ (Co-O) bonding [52, 53]. However, the peak intensities of $Co^{3+}$ peaks at 779.1 and 781.2 eV are more than that of the $Co^{2+}$ present at 780.5 and 797 eV. Furthermore, as shown in Fig. S8(c) the oxygen (O1s) peak is deconvoluted into three peaks at the binding energy of 530.8, 532.3, and 533.2 eV, respectively. These observed binding energy peaks are attributed to the lattice oxygen of metal oxide, OH species on the surface, and the 533.2 can be related to the adsorbed water near the surface [54,55]. Furthermore, the high resolution XPS spectrum of Fe 2p, Zr 3d does not show any significant difference that that of the Fig. 2((b) and (d)) and Fig. S8(d), (e). As shown in the Fig. S8(f) the presence of Sn $3d_{5/2}$ and Sn $3d_{3/2}$ peaks at 487.3 and 496.1 eV, is attributed to $Sn^{4+}$ state. Thus, the results of XPS analysis clearly demonstrate the formation of $Co_2O_3$-CoO (further termed as $CoO_x$) on the surface of FeOOH/Zr-$Fe_2O_3$ NC photoanodes.

However, it is expected that the amount of $CoO_x$ loading on the AT-12/Zr-$Fe_2O_3$ NC had a trivial effect on the OER performance. Therefore, to confirm the presence of cobalt oxide loading on the surface of the photoanodes, cyclic voltammetry was performed. The cyclic voltammograms clarified the surface property of the $CoO_x$-loaded Zr-$Fe_2O_3$ NC in the presence of an acid-treated intermediate state. The cathodic process represents the adsorption of Co, and the positive sweep in cyclic voltammetry represents the oxidation of adsorbed atomic Co formed in the cathodic scan [56, 57]. The larger area under the curve for $CoO_x$/AT-12/Zr-$Fe_2O_3$ NC indicates greater loading of $CoO_x$ on the surface of the AT-12/Zr-

$Fe_2O_3$ NC electrode (Fig. S9(a)). To further support the charge recombination at the hematite/electrolyte interface and the water oxidation dynamics, photocurrent transient measurements of $CoO_x$/AT-12/Zr-$Fe_2O_3$ NC and $CoO_x$/Zr-$Fe_2O_3$ were performed at 0.75 V vs. HgO/HgO in a 1 M NaOH aqueous electrolyte. Anodic transient photocurrent spikes increased within the first second of irradiation for both the $CoO_x$/Zr-$Fe_2O_3$ NC and $CoO_x$/AT-12/Zr-$Fe_2O_3$ NC photoanodes, as shown in Fig. S9(b). The increased spike for $CoO_x$/Zr-$Fe_2O_3$ was owing to the storage of photogenerated holes at the interface, suggesting slower OER kinetics [56]. When the light was turned off, the cathodic transient peak was observed, which was attributed to electrons diffusing from the external circuit and recombining with the stored holes at the semiconductor-liquid junction [58]. The reduced transient peak after the acid treatment between $CoO_x$ and Zr-$Fe_2O_3$ NC in $CoO_x$/AT-12/Zr-$Fe_2O_3$ NC photoanodes is because of reduced surface recombination and larger proportion of holes had sufficient potential to oxidize water [59]. It has been reported that the transient photocurrents of crystalline $Fe_2O_3$ were significantly higher than those of amorphous $Fe_2O_3$ [60]; therefore, the decrease in the transient photocurrents of $CoO_x$/AT-12/Zr-$Fe_2O_3$ NC possibly resulted from the presence of amorphous FeOOH on the surface, as indicated by the XPS results. The dark currents for water oxidation on the $CoO_x$/Zr-$Fe_2O_3$ NC and $CoO_x$/AT-12/Zr-$Fe_2O_3$ NC electrodes were measured, as shown in Fig. S9(c). The cathodic dark onset potential of the $CoO_x$/AT-12/Zr-$Fe_2O_3$ NC indicated a higher electrocatalytic activity for water oxidation compared with the $CoO_x$/Zr-$Fe_2O_3$ NC, in agreement with the cathodic shift of the photocurrent onset potential [61]. Additionally, open-circuit voltage measurements indicated the formation of a built-in electric field [62]. Fig. S9(d) shows the change in the OCP (ΔOCP) vs. the light illumination time. Under illumination, all the photoanodes exhibited a negative shift compared with the dark condition, confirming a rapid shift of the Fermi level to more cathodic potentials. When the light was turned off, the accumulated electrons inside the NCs were redistributed owing to charge recombination until the Fermi level of the photoanodes reached a new level, resulting in a gradual reduction in $V_{oc}$ to the original level [63]. Compared with the Zr-$Fe_2O_3$ NC, AT-12/Zr-$Fe_2O_3$ NC, and $CoO_x$/Zr-$Fe_2O_3$ NC photoanodes, the $CoO_x$/AT-12/Zr-$Fe_2O_3$ NC photoanode exhibited a significantly larger ΔOCP, indicating less recombination of electron-hole pairs. The field-emission SEM (FESEM) and FESEM-EDS mapping images of the optimum $CoO_x$-encapsulated acid-treated Zr-$Fe_2O_3$ NC photoanode are shown in Fig. S10(a)-(f), respectively. The FESEM- EDS mapping of optimum $CoO_x$-encapsulated acid-treated Zr-$Fe_2O_3$ NC shows the uniform elemental distribution of Co, O, Zr, and Fe. Corresponding energy-dispersive X-ray spectroscopy (EDX) profile of whole areas (1 μm) of the optimum $CoO_x$-encapsulated acid-treated Zr-$Fe_2O_3$ NC photoanodes is shown in Fig. S10(g). The EDS displays the presence of the Co, O, Fe, Zr, and Sn peaks.

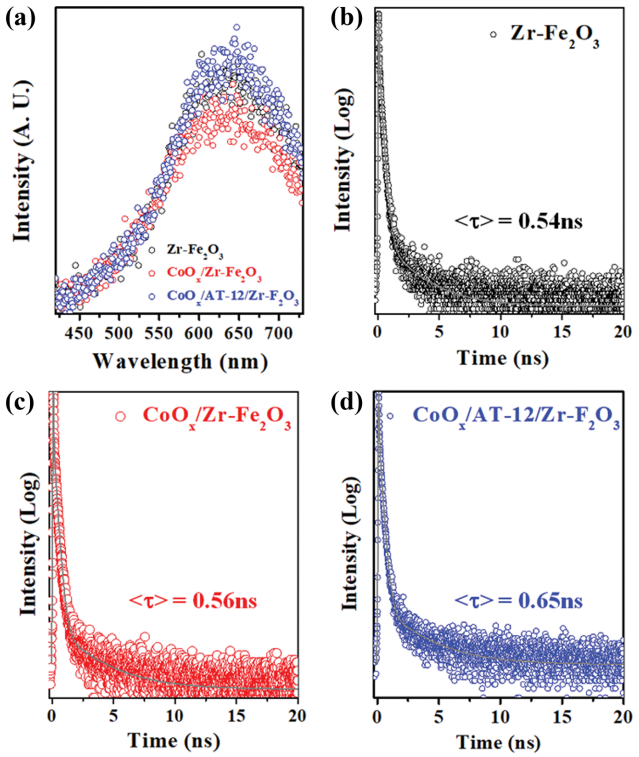



**Fig. 6 (a) Steady-state PL spectra and (b)-(d) TRPL decay of the Zr-$Fe_2O_3$ photoanodes with/without $CoO_x$ : Zr-doped hematite (black), Zr-doped hematite with $CoO_x$ (red), and Zr-doped hematite with acid-treated $CoO_x$ (blue). The excitation source was a 379-nm pulsed laser.**

Fig. 6 shows the TRPL characteristics of the Zr-$Fe_2O_3$, $CoO_x$/Zr-$Fe_2O_3$, and $CoO_x$/AT-12/Zr-$Fe_2O_3$ photoanodes. Photoelectrochemical reactions are strongly related with the photogenerated charge-carrier kinetics in excited electronic states [64]. The charge-carrier kinetics can be evaluated according to the measured PL lifetime after irradiation with a short laser pulse. Fig. 6(a)-(d) shows the PL decay with respect to time in the nanosecond time regime. The observed PL spectrum indicated broad emissions in the red spectral region. The PL intensity was slightly modulated with and without $CoO_x$ and acid treatment. To analyze the quantitative recombination characteristics of the photoexcited charge carriers, we measured the TRPL for the doped hematite phases. The observed PL decays were reasonably fitted by three lifetime sub-components, as shown in Table 2, indicating that multiple recombination pathways exist in such complex doped materials, as expected. The deconvoluted lifetime consisted of 0.03, 0.27, and 2.8 ns in the Zr-doped hematite phase. When the Zr-doped hematite was modified with

**Table 2. PL lifetime parameters of the examined photoanodes**

| Sample | $A_1$ (%) | $\tau_1$ (ns) | $A_2$ (%) | $\tau_2$ (ns) | $A_3$ (%) | $\tau_3$ (ns) | $<\tau>^a$ (ns) |
|---|---|---|---|---|---|---|---|
| Zr-$Fe_2O_3$ | 78.1 | 0.03 | 21.4 | 0.27 | 0.5 | 2.8 | 0.54 |
| $CoO_x$/Zr-$Fe_2O_3$ | 81.6 | 0.03 | 18.1 | 0.27 | 0.3 | 3.4 | 0.56 |
| $CoO_x$/AT-12/Zr-$Fe_2O_3$ | 82.0 | 0.03 | 17.6 | 0.27 | 0.4 | 3.4 | 0.65 |

$CoO_x$, the PL lifetime consisted of similar short lifetimes ($\tau_1$ and $\tau_2$), except for the longest lifetime ($\tau_3$), which increased to 3.4 ns. Interestingly, the amplitude of $\tau_1$ was increased by 81.6% compared with that of the Zr-$Fe_2O_3$ NC (78.1%). Considering the fastest lifetime component ($\tau_1$), which typically includes nonradiative processes such as charge transfer, trapping, and/or transport [65]. The charge carriers excited in the $CoO_x$/Zr-doped hematite underwent slightly more contribution from nonradiative recombination in addition to the delayed lifetime ($\tau_3$). Thus, it is considered that the doped photoanode materials used in this study could enhance the charge transfer and transport, as well as charge separation, simultaneously after acid treatment and $CoO_x$ modification.

### 3. PEC Water Splitting and Role of Cobalt Oxide-encapsulation on Acid-treated $Fe_2O_3$ Photoanodes

The optimum highly stable $CoO_x$/AT-12/Zr-$Fe_2O_3$ photoanode was used for PEC water-splitting measurements. The PEC stability and corresponding stability during PEC water splitting ($H_2$ and $O_2$ evolution) over the $CoO_x$/AT-12/Zr-$Fe_2O_3$ photoanode were detected via GC and plotted with respect to time, as shown in Fig. 7. As indicated by the *J-t* curves, the $CoO_x$/AT-12/Zr-$Fe_2O_3$ photoanode exhibited only a 2% decrement in the photocurrent density under continuous 10 h irradiation at 1.23 V vs. RHE, indicating its superior stability in 1 M NaOH electrolyte. The amount of $H_2$ and $O_2$ evolution over the $CoO_x$/AT-12/Zr-$Fe_2O_3$ photoanode after 10 h was calculated to be ~225 and 105 μmol/$cm^2$, respectively. Fig. S11 displays, after 10 h of continuous illumination, the $CoO_x$/AT-12/Zr-$Fe_2O_3$ photoanode exhibits Faradaic efficiency of the $H_2$ and $O_2$ evolution over 65 to 75%, respectively. This might be due to side reactions in solution or reduction/oxidation of the electrode material or surface species. Additional likely cause for the low value of faradaic efficiency is, partially, gas leakage during the experimental process (sampling and manual injection into the GC) [66].

On the basis of the experimental results, we proposed the charge-transfer mechanism for the $CoO_x$-loaded acid-treated Zr-$Fe_2O_3$ NC photoanodes (Fig. 8). In this study, in addition to the light-absorption effect, the enhanced PEC performance of the $CoO_x$/AT-12/Zr-$Fe_2O_3$ photoanodes was mainly attributed to the reduced charge-carrier recombination. The presence of $CoO_x$ in the Zr-$Fe_2O_3$ photoanodes (both with and without acid treatment) catalyzed the water-splitting process, allowing it to proceed at a low overpotential [64]. Additionally, the presence of a thin layer of FeOOH on the surface of the Zr-$Fe_2O_3$ NC functioned as an $O_2$-evolution cocatalyst (interlayer) for photogenerated holes and transferred them to $CoO_x$ [66]. Furthermore, the amount of $CoO_x$ on the acid-treated Zr-$Fe_2O_3$ NC led to charge acceleration at the electrode/electrolyte interface and thus reduced the electron-hole recombination rate compared with the $CoO_x$/Zr-$Fe_2O_3$ NC photoanodes. As indicated by the EIS and surface charge-transfer efficiency results,

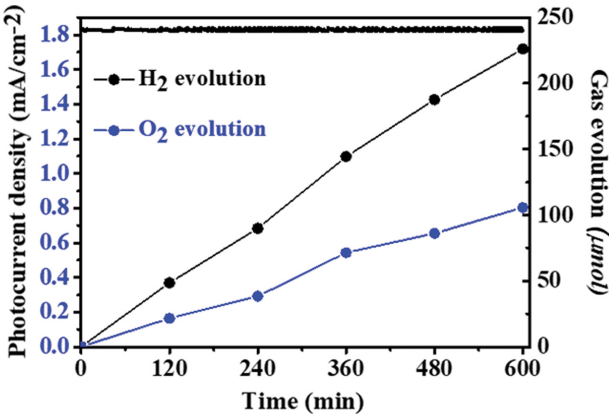



**Fig. 7. Photoelectrochemical stability and photoelectrochemical water splitting over $CoO_x$/AT-12/Zr-$Fe_2O_3$ photoanodes at 1.23 V vs. RHE.**

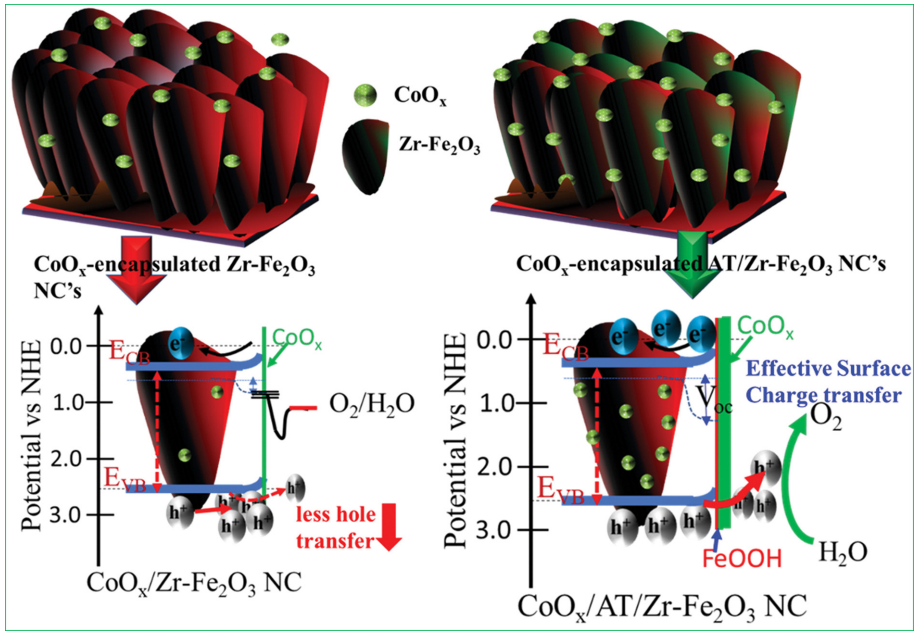



**Fig. 8. Charge-transfer kinetics in $CoO_x$/AT-12/Zr-$Fe_2O_3$ photoanodes during the PEC water splitting under one sun illumination condition.**

the $CoO_x$ layer in acid-treated Zr-$Fe_2O_3$ enhanced the surface charge transfer, and additional band bending occurred at the electrode/electrolyte interface compared with the $CoO_x$/Zr-$Fe_2O_3$ NC photoanodes [67]. Thus, the synergistic effects of the acid treatment and $CoO_x$ reduced the charge-transfer barrier and accelerated the transfer of charge carriers across the electrode/electrolyte interface, improving the water-splitting activity of the $CoO_x$/AT-12/Zr-$Fe_2O_3$ NC photoanodes.

## CONCLUSIONS

The synergistic effect of acid treatment and $CoO_x$ loading on the cathodic shift in the onset potential and the performance of Zr-doped $Fe_2O_3$ NC photoanodes was examined. XPS analyses confirmed that the surface of the Zr-$Fe_2O_3$ NC photoanode was modified with the FeOOH after the acid treatment. Mott-Schottky and EIS analyses confirmed that the photocurrent improvement was due to the donor density and efficient charge transfer at the acid-treated Zr-$Fe_2O_3$ NC photoanode/electrode interface. XPS and surface charge-transfer efficiency results indicated that the formation of the FeOOH $O_2$-evolution cocatalyst in the acid-treated Zr-$Fe_2O_3$ NC facilitated the transfer of holes from the VB of the electrode to the electrolyte. $CoO_x$-loaded acid-treated Zr-$Fe_2O_3$ exhibited a 200-mV cathodic shift of the onset potential with a 1.83 $mA/cm^2$ photocurrent density at 1.23 V vs. RHE. PL analyses provided evidence for the passivation effect after the acid treatment and $CoO_x$ loading of the Zr-$Fe_2O_3$ NC photoanodes. Our strategy of acid treatment and $CoO_x$ loading of Zr-$Fe_2O_3$ NC can be used to design effective PEC systems with manifold functional components and for other energy-conversion applications.

## ACKNOWLEDGEMENTS

This research was supported by the BK21 plus program and a National Research Foundation of Korea (NRF) grant funded by the Korean government (MSIT) (No. 2019R1A2C1006402). It was also supported by the Brain Pool Program through the National Research Foundation of Korea (NRF) funded by the Ministry of Science and ICT (2017H1D3A1A02014020). Also. this research was supported by Research Base Construction Fund Support Program funded by Chonbuk National University in 2020.

## SUPPORTING INFORMATION

Additional information as noted in the text. This information is available via the Internet at http://www.springer.com/chemistry/journal/11814.

## REFERENCES

1. A. Kudo and Y. Miseki, *Chem. Soc. Rev.*, **38**, 253 (2009).
2. J. Hu, Y. Ji, Z. Mo, N. Li, Q. Xu, Y. Li, H. Xu, D. Chen and J. Lu, *J. Mater. Chem. A*, **7**, 4408 (2019).
3. F. L. Formal, K. Sivula and M. Gratzel, *J. Phys. Chem. C*, **116**, 26707 (2012).
4. F. L. Formal, S. R. Pendlebury, M. Cornuz, S. D. Tilley, M. Gratzel and J. R. Durrant, *J. Am. Chem. Soc.*, **136**, 2564 (2014).
5. M. J. Katz, S. C. Riha, N. C. Jeong, A. B. F. Martinson, O. K. Farha and J. T. Hupp, *Coord. Chem. Rev.*, **256**, 2521 (2012).
6. Gurudayal, D. Sabba, M. H. Kumar, L. H. Wong, J. Barber, M. Grätzel and N. Mathews, *Nano Lett.*, **15**, 3833 (2015).
7. R. Franking, L. Li, M. A. Lukowski, F. Meng, Y. Tan, R. J. Hamers and S. Jin, *Energy Environ. Sci.*, **6**, 500 (2013).
8. Y. W. Phuan, E. Ibrahim, M. N. Chong, T. Zhu, B. K. Lee, J. D. Ocon and E. S. Chan, *Appl. Surf. Sci.*, **392**, 144 (2017).
9. K. Sivula, F. Le Formal and M. Grätzel, *ChemSusChem*, **4**, 432 (2011).
10. G. M. Carrolla and D. R. Gamelin, *J. Mater. Chem. A*, **4**, 2986 (2016).
11. P. Kuang, L. Zhang, B. Cheng and J. Yu, *Appl. Catal. B-Environ.*, **218**, 570 (2017).
12. L. Qin, M. Liu, Y. Wu, Z. Xu, X. Guo and G. Zhang, *Appl. Catal. B: Environ.*, **194**, 50 (2016).
13. Z. Luo, T. Wang, J. Zhang, C. Li, H. Li and J. Gong, *Angew. Chem., Int. Ed.*, **56**, 12878 (2017).
14. J. W. Jang, C. Du, Y. Ye, Y. Lin, X. Yao, J. Thorne, E. Liu, G. McMahon, J. Zhu, A. Javey, J. Guo and D. Wang, *Nat. Commun.*, **6**, 7447 (2015).
15. T. Hisatomi, F. Le Formal, M. Cornuz, J. Brillet, N. Tetreault, K. Sivula and M. Gratzel, *Energy Environ. Sci.*, **4**, 2512 (2011).
16. S. J. A. Moniz, S. A. Shevlin, D. J. Martin, Z.-X. Guo and J. Tang, *Energy Environ. Sci.*, **8**, 731 (2015).
17. D. Cao, W. Luo, J. Feng, X. Zhao, Z. Lia and Z. Zou, *Energy Environ. Sci.*, **7**, 752 (2014).
18. I. S. Cho, H. S. Han, M. Logar, J. Park and X. Zheng, *Adv. Energy Mater.*, **6**, 1501840 (2016).
19. Y. Yang, M. Forster, Y. Ling, G. Wang, T. Zhai, Y. Tong, A. J. Cowan and Y. Li, *Angew. Chem. Int. Ed.*, **55**, 3403 (2016).
20. F. Malara, A. Minguzzi, M. Marelli, S. Morandi, R. Psaro, V. Dal Santo and A. Naldoni, *ACS Catal.*, **5**, 5292 (2015).
21. K. Sun, M. T. McDowell, A. C. Nielander, S. Hu, M. R. Shaner, F. Yang, B. S. Brunschwig and N. S. Lewis, *J. Phys. Chem. Lett.*, **6**, 592 (2015).
22. Y. S. Hu, A. K. Shwarsctein, G. D. Stucky and E. W. McFarland, *Chem. Commun.*, 2652 (2009).
23. A. Subramanian, M. A. Mahadik, J. W. Park, I. K. Jeong, H. S. Chung, H. H. Lee, S. H. Choi, W. S. Chae and J. S. Jang, *Electrochim. Acta*, **319**, 444 (2019).
24. P. Zhang, T. Wang, X. X. Chang, L. Zhang and J. L. Gong, *Angew. Chem. Int. Ed.*, **55**, 5851 (2016).
25. S. R. Kim, M. A. Mahadik, W. S. Chae, J. Ryu, S. H. Choi and J. S. Jang, *Appl. Surf. Sci.*, **513**, 145528/1 (2020).
26. Y. Park, K. J. McDonald and K. S. Choi, *Chem. Soc. Rev.*, **42**, 2321 (2013).
27. I. K. Jeong, M. A. Mahadik, J. B. Hwang, W. Chae, S. H. Choi and J. S. Jang, *J. Colloid Interface Sci.*, **581**, 751 (2021).
28. J. Brillet, J. H. Yum, M. Cornuz, T. Hisatomi, R. Solarska, J. Augustynski, M. Grätzel and K. Sivula, *Nat. Photonics*, **6**, 824 (2012).
29. J. Brillet, M. Cornuz, F. Le Formal, J. H. Yum, M. Grätzel and K. Sivula, *J. Mater. Res.*, **25**, 17 (2010).
30. D. Chen and Z. Liu, *ChemSusChem*, **11**, 3438 (2018).
31. M. A. Mahadik, H. S. Chung, S. Y. Lee, M. Cho and J. S. Jang, *ACS Sustain. Chem. Eng.*, **6**, 12489 (2018).

32. G. Wang, H. Wang, Y. Ling, Y. Tang, X. Yang, R. Fitzmorris, C. Wang, J. Zhang and Y. Li, *Nano Lett.*, **11**, 3026 (2011).
33. L. Xi, S. Chiam, W. Mak, P. Tran, J. Barber, S. Loo and L. Wong, *Chem. Sci.*, **4**, 164 (2013).
34. T. Jeon, W. Choi and H. Park, *J. Phys. Chem. C*, **115**, 7134 (2011).
35. P. Kumar, P. Sharma, A. G. Joshi, R. Shrivastav, S. Dass and V. R. Satsangi, *J. Electrochem. Soc.*, **159**, 685 (2012).
36. J. W. Park, M. A. Mahadik, G. W. An, S. Y. Lee, P. G. Choi, S. H. Chae, W. S. Chung, H. H. S. S. Park and J. S. Jang, *Sol. Energy Mater. Sol. Cells*, **187**, 207 (2018).
37. M. A. Mahadik, A. Subramanian, H. S. Chung, J. Ryu, M. Cho and J. S. Jang, *ChemSusChem.*, **10**, 2030 (2017).
38. J. W. Park, M. A. Mahadik, H. Ma, G. W. An, H. Lee, S. H. Choi, W. Chae, H. Chung and J. S. Jang, *ACS Sustain Chem. Eng.*, **7**, 6947 (2019).
39. G. Wang, Y. Ling, H. Wang, L. Xihong and Y. Li, *J. Photochem. Photobiol., C*, **19**, 35 (2014).
40. P. S. Shinde, S. H. Choi, Y. Kim, J. Ryu and J. S. Jang, *Phys. Chem. Chem. Phys.*, **18**, 2495 (2016).
41. C. Ding, Z. Wang, J. Shi, T. Yao, A. Li, P. Yan, B. Huang and C. Li, *ACS Appl. Mater. Interfaces*, **8**, 7086 (2016).
42. P. Qiu, H. Yang, L. Yang, Q. Wang and L. Ge, *Electrochim. Acta*, **266**, 431 (2018).
43. M. A. Mahadik, P. S. Shinde, M. Cho and J. S. Jang, *Appl. Catal. B-Environ.*, **184**, 337 (2016).
44. P. Y. Tang, L. J. Han, F. S. Hegner, P. Paciok, M. Biset-Peiró, H. C. Du, X. K. Wei, L. Jin, H. B. Xie, Q. Shi, T. Andreu, M. Lira-Cantú, M. Heggen, R. E. Dunin-Borkowski, N. López, J. R. Galán-Mascarós, J. R. Morante and J. Arbiol, *Adv. Energy Mater.*, **9**, 1901836 (2019).
45. D. Monllor-Satoca, M. Bärtsch, C. Fàbrega, A. Genç, S. Reinhard, T. Andreu, J. Arbiol, M. Niederberger and J. R. Morante, *Energy Environ. Sci.*, **8**, 3242 (2015).
46. B. Klahr, S. Gimenez, F. Fabregat-Santiago, T. Hamann and J. Bisquert, *J. Am. Chem. Soc.*, **134**, 4294 (2012).
47. P. Y. Tang and J. Arbiol, *Nanoscale Horiz.*, **4**, 1256 (2019).
48. P. Y. Tang, H. B. Xie, C. Ros, L. J. Han, M. Biset-Peiró, Y. M. He, W. Kramer, A. P. Rodríguez, E. Saucedo, J. R. Galán-Mascarós, T. Andreu, J. R. Morante and J. Arbiol, *Energy Environ. Sci.*, **10**, 2124 (2017).
49. F. Li, J. Li, J. Zhang, L. Gao, X. Long, Y. Hu, S. Li, J. Jin and J. Ma, *ChemSusChem*, **11**, 2156 (2018).
50. K. G. U. Wijayantha, S. Saremi-Yarahmadi and L. M. Peter, *Phys. Chem. Chem. Phys.*, **13**, 5264 (2011).
51. L. Xia, J. Bai, J. Li, Q. Zeng, L. Li and B. Zhou, *Appl. Catal. B-Environ.*, **204**, 127 (2017).
52. M. Liu, Y. Hao, L. Zheng, L. Niu and D. Miao, *J. Mater. Eng. Perform.*, **28**, 1 (2019).
53. K. Jiratova, R. Perekrestov, M. Dvorakova, J. Balabanova, P. Topka, M. Kostejn, J. Olejnicek, M. Cada, Z. Hubicka and F. Kovanda, *Catalysts*, **9**, 806 (2019).
54. P. Arunachalam, M. N. Shaddad, A. S. Alamoudi, M. A. Ghanem and A. M. Al-Mayouf, *Catalysts*, **7**, 119 (2017).
55. S. Mandal, M. Rakibuddin and R. Ananthakrishnan, *ACS Omega*, **3**, 648 (2018).
56. T. C. Gentil, V. S. Pinheiro, E. C. Paz, F. M. Souza, L. S. Parreira and M. C. Santos, *J. Braz. Chem. Soc.*, **30**, 1634 (2019).
57. S. A. Rasaki, Z. Chen, H. Shen, H. Guo, T. Thomas and M. Yang, *Electrocatalysis*, **11**, 579 (2020).
58. C. Sanchez, K. D. Sieber and G. A. Somorjai, *J. Electroanal. Chem.*, **252**, 269 (1988).
59. F. L. Formal, N. Tétreault, M. Cornuz, T. Moehl, M. Grätzel and K. Sivula, *Chem. Sci.*, **2**, 737 (2011).
60. M. Zhang, W. Luo, N. Zhang, Z. Li, T. Yu and Z. Zou, *Electrochem. Commun.*, **23**, 41 (2012).
61. F. A. Benko, J. Longo and F. P. Koffyberg, *J. Electrochem. Soc.*, **132**, 609 (1985).
62. Y. Zhang, S. Jiang, W. Song, P. Zhou, H. Ji, W. Ma, W. Hao, C. Chen and J. Zhao, *Energy Environ. Sci.*, **8**, 1231 (2015).
63. F. Li, J. Li, F. Li, L. Gao, X. Long, Y. Hu, C. Wang, S. Wei, J. Jin and J. Ma, *J. Mater. Chem. A*, **6**, 13412 (2018).
64. P. Li, Z. Jin and D. Xiao, *J. Mater. Chem. A*, **2**, 18420 (2014).
65. L. Wang, Y. Yang, Y. Zhang, Q. Rui, B. Zhang, Z. Shen and Y. Bi, *J. Mater. Chem. A*, **5**, 17056 (2017).
66. Gurudayal, S. Y. Chiam, M. H. Kumar, P. S. Bassi, H. L. Seng, J. Barber and L. H. Wong, *ACS Appl. Mater. Interfaces*, **6**, 5852 (2014).
67. G. Ai, R. Mo, H. Li and J. Zhong, *Nanoscale*, **7**, 6722 (2015).

## Supporting Information

# Engineering of cobalt oxide-integrated nitric acid-functionalized Zr-$Fe_2O_3$ nanocoral photoanodes for photoelectrochemical water splitting

**Jun Beom Hwang*, Sarang Kim*, Weon-Sik Chae**, Habib Mohiddin Pathan***, Mahadeo Abasaheb Mahadik*,†, and Jum Suk Jang*,†**

*Division of Biotechnology, Safety, Environment and Life Science Institute, College of Environmental and Bioresource Sciences, Chonbuk National University, Iksan 54596, Korea

**Daegu Center, Korea Basic Science Institute, Daegu 41566, Korea

***Advanced Physics Laboratory, Department of Physics, Savitribai Phule Pune University, Pune-411007, India

(*Received 26 October 2020 • Revised 18 January 2021 • Accepted 26 January 2021*)

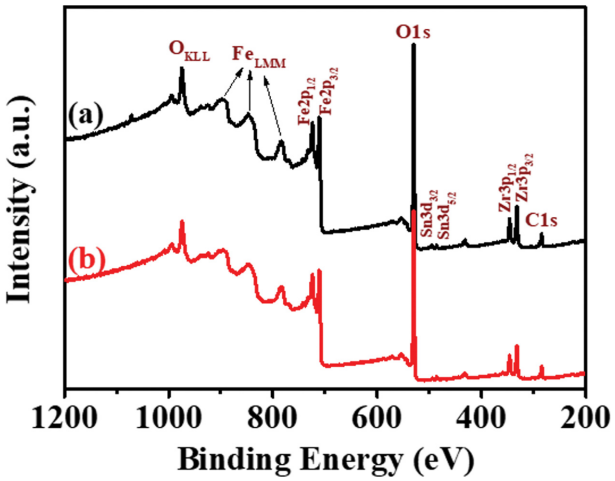



**Fig. S1. XPS survey scan spectra of (a) Zr-$Fe_2O_3$, and (b) AT-12/Zr-$Fe_2O_3$ photoanodes a survey spectrum.**

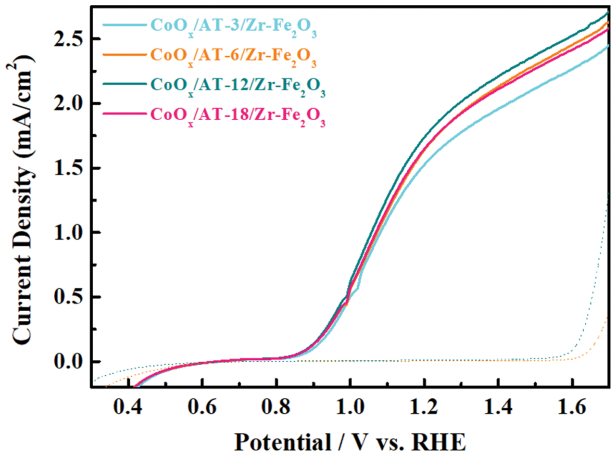



**Fig. S2. *J-V* curves of acid treated $CoO_x$ loaded Zr-$Fe_2O_3$ photoanodes prepared at various acid treatment time (3, 6, 12 and 18 hr, respectively). Electrolyte: 1 M NaOH electrolyte and Light illumination-1 sun standard illumination conditions.**

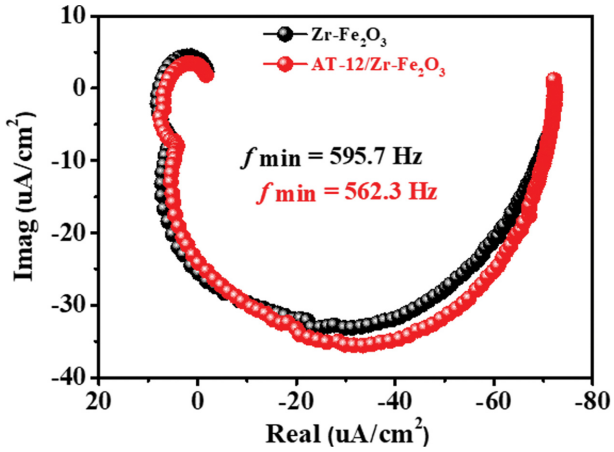



**Fig. S3. IMPS spectra of bare Zr-$Fe_2O_3$ NC and AT-12/Zr-$Fe_2O_3$ NC photoanodes measured at 1.23 V vs Hg/HgO using a green light emitting diode (LED, peak wavelength 520 nm) driven by a frequency-response analyzer. The frequency was swept from 10 kHz down to 0.1 Hz with the 10% light intensity modulation.**

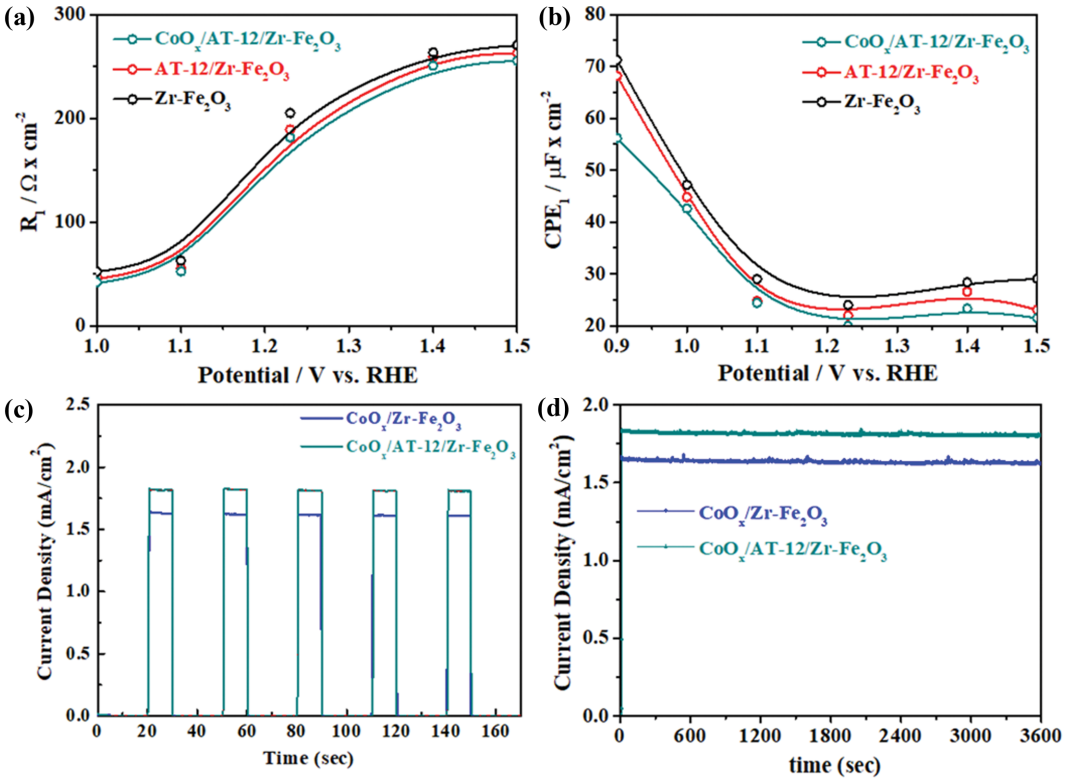



Fig. S4. (a), (b) bulk resistances ($R_1$) and associated capacitances ($CPE_1$) of $Zr\text{-}Fe_2O_3$, $AT\text{-}12/Zr\text{-}Fe_2O_3$ and $CoO_x/AT\text{-}12/Zr\text{-}Fe_2O_3$ at different applied potentials obtained upon fitting their respective Nyquist plots to the equivalent circuit (c) transient photocurrent responses under one sun chopped light conditions; (d) photocurrent stability of $CoO_x/Zr\text{-}Fe_2O_3$ (blue) and $CoO_x/AT\text{-}12/Zr\text{-}Fe_2O_3$ (dark cyan) photoanodes in a 1 M NaOH electrolyte at 1.23 V vs. RHE.

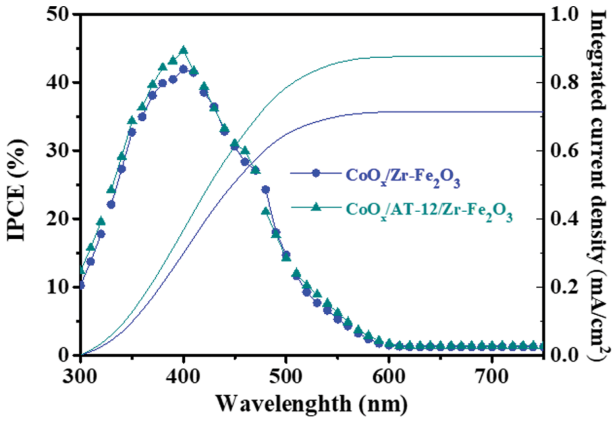



Fig. S5. IPCE spectra for $CoO_x/Zr\text{-}Fe_2O_3$ (blue), $CoO_x/AT\text{-}12/Zr\text{-}Fe_2O_3$ (dark cyan) photoanodes in a 1 M NaOH electrolyte at 1.23 V vs. RHE.

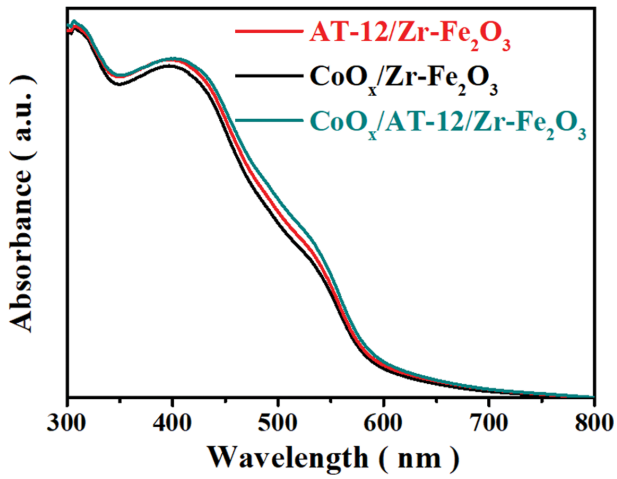



Fig. S6. UV DRS absorption spectra of $AT\text{-}12/Zr\text{-}Fe_2O_3$ NC, $CoO_x/Zr\text{-}Fe_2O_3$ NC and $CoO_x/AT\text{-}12/Zr\text{-}Fe_2O_3$ NC photoanodes.

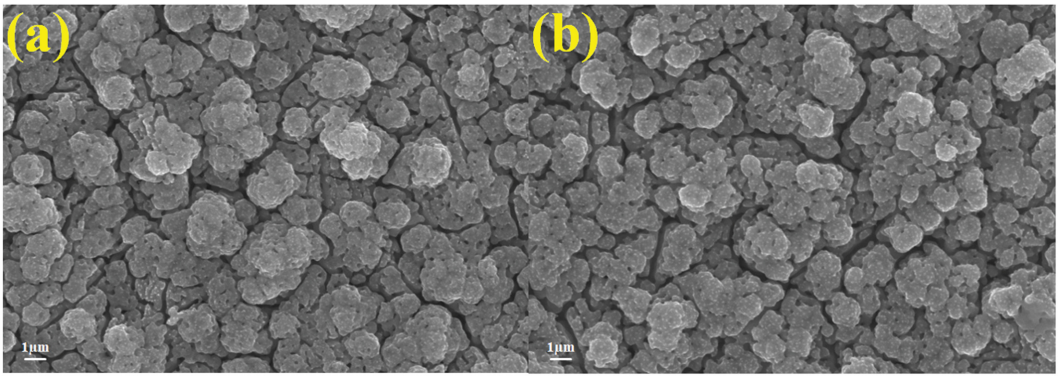



**Fig. S7. Top-view FESEM images of (a) $CoO_x$/Zr-$Fe_2O_3$ NC and (b) CoO/AT-12/Zr-$Fe_2O_3$ NC photoanodes, respectively.**

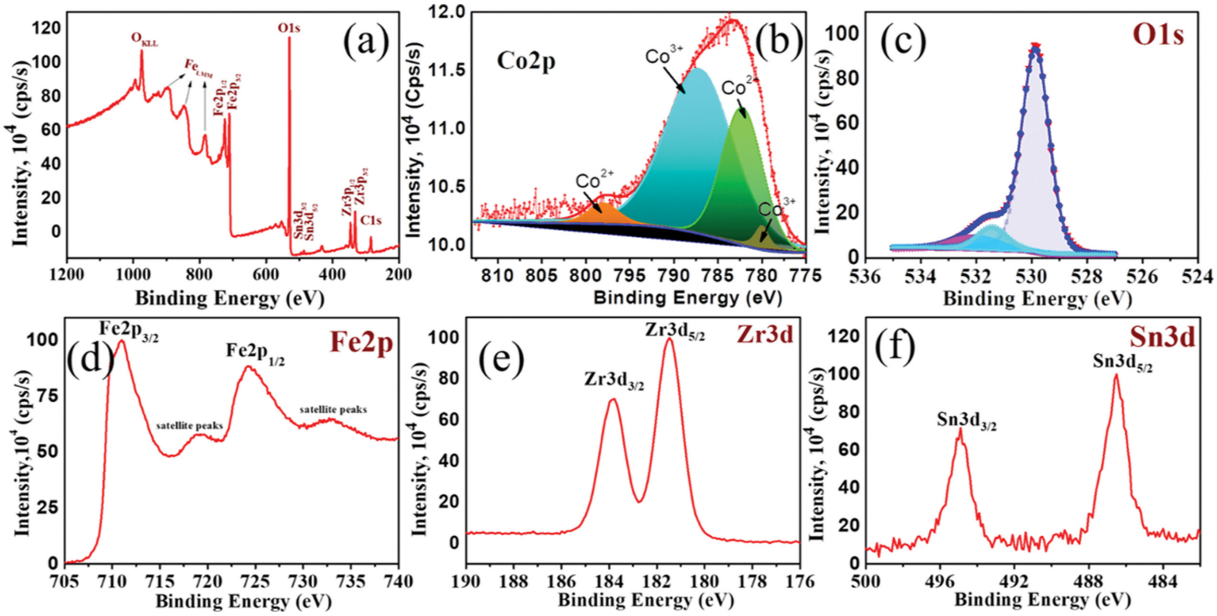



**Fig. S8. (a) XPS survey scan, (b)-(f) High resolution XPS scan of Co2p, O1s, Fe 2p, Zr 3d and Sn 3d for optimum $CoO_x$/AT-12/Zr-$Fe_2O_3$ NC photoanode.**

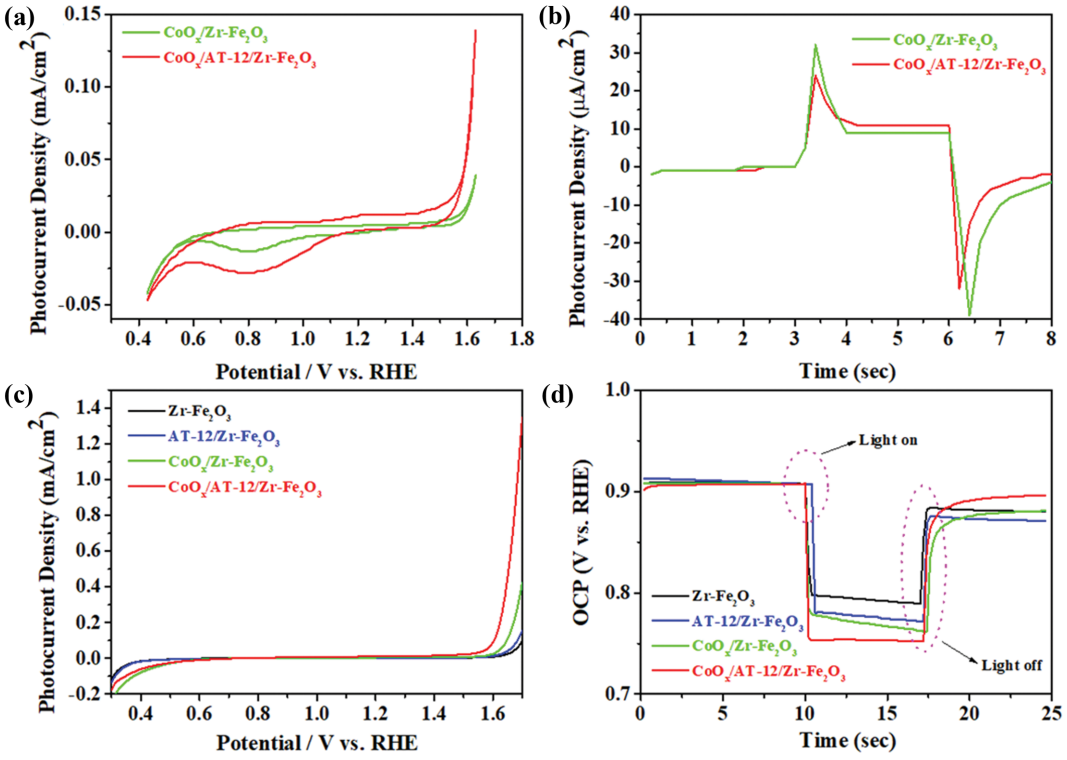



Fig. S9. (a) CV analysis for $CoO_x/Zr\text{-}Fe_2O_3$ NC and $CoO_x/AT\text{-}12/Zr\text{-}Fe_2O_3$ NC (The scan rate=50 $mV{\cdot}s^{-1}$), (b) transient photocurrent of the $CoO_x/Zr\text{-}Fe_2O_3$ NC and $CoO_x/AT\text{-}12/Zr\text{-}Fe_2O_3$ NC at applied potential of 0.83 V vs Hg/HgO, (c) dark current for water oxidation and (d) open circuit voltage decay curves of pure $Zr\text{-}Fe_2O_3$ NC, acid treated $Zr\text{-}Fe_2O_3$ NC, $CoO_x/Zr\ Fe_2O_3$ and $CoO_x/AT\text{-}12/Zr\text{-}Fe_2O_3$ NC electrode respectively.

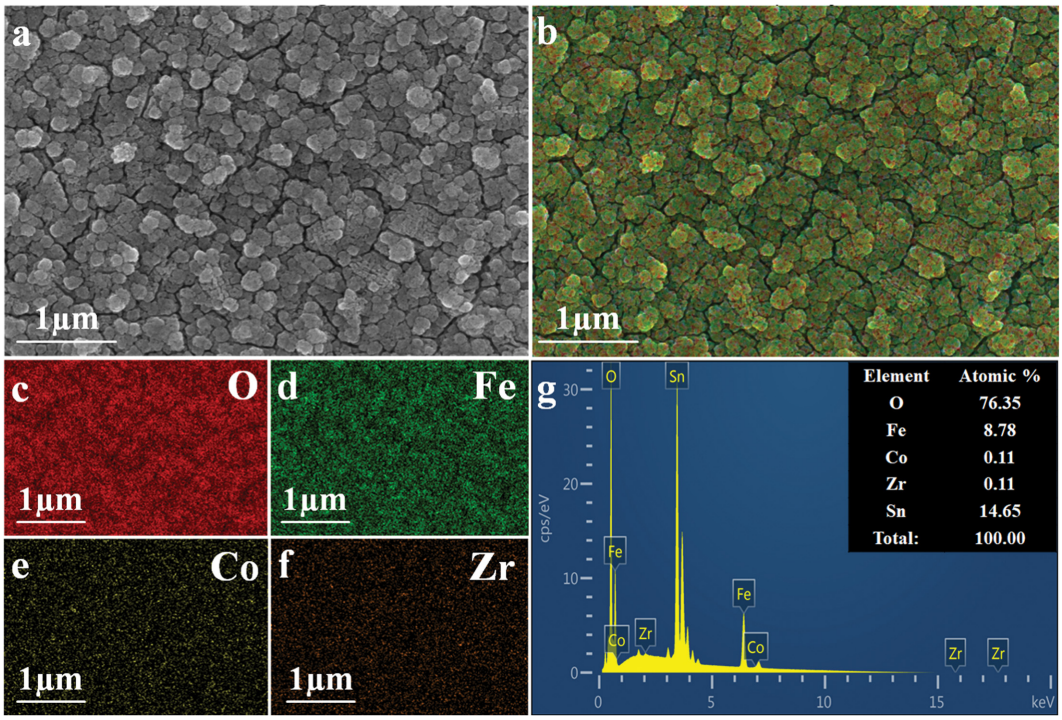



Fig. S10. (a) FESEM and (b)-(f) corresponding FESEM-EDS elemental mapping images for optimum $CoO_x$-encapsulated acid-treated $Zr\text{-}Fe_2O_3$ NC photoanodes, (g) EDS spectrum and inset shows the elemental composition tables of Fig. S10(g).

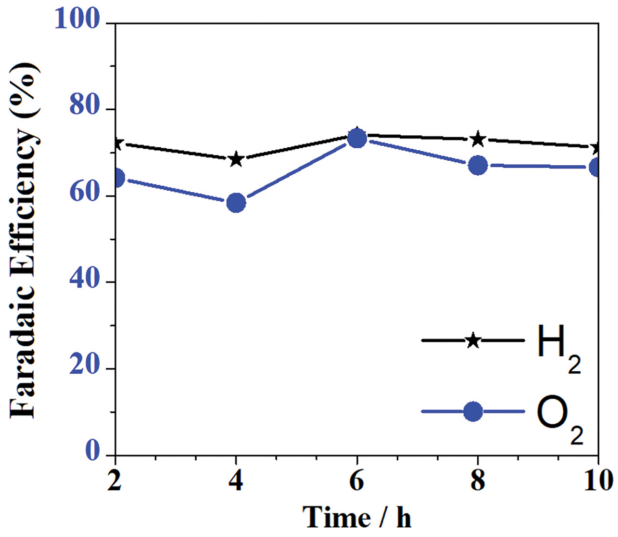



**Fig. S11. Faradaic efficiency as a function of time for the optimized $CoO_x$/AT-12/Zr-$Fe_2O_3$ photoanode under 1 sun illumination in the 1 M NaOH electrolyte (pH~13.8).**